Supporting information

Regulating the Local Electronic Structure to design Reliable Dual-Active Site Organic Anode compatible with High-Performance Lithium-Ion Batteries

Changjian Zhang[#a], Chengwei Li[#a], Yun Huang[*a], Yunhe Zhang[a], Jie Xiao[a], Caixia Li[a], Yanzhou Wang[a], Xichang Wang[a], Xing Li[a], Mingshan Wang[a], Yuanhua Lin[a], Haijun Cao[*b]

---

[*] Corresponding author. Tel.: +86 28 83037409
[#] The two authors contributed equally.
E-mail address: huangyun982@163.com (Y. Huang)
chj007@163.com (H.J. Cao)

SnPA-based electrode after 100 cycles. (f) Rate charge-discharge curves. (g) Rate performance of SnPA. (h) Long-cycle performance of the SnPA anode at 500 mA $g^{-1.}$

Fig. S16. Long-cycle performance of Fe_2PA_3 electrode (a) at 0.1 A g^{-1}. (b) Long-cycle performance at 0.2 A g^{-1}. (c) Rate performance. (d) Long-cycle performance at 1 A g^{-1}. (e) Long-cycle performance at 2 A g^{-1}. (f) Long cycles at 5 A g^{-1}.

Fig. S17. SEM images of MnPA electrode (a-c) before test, (d-f) after 15 cycles, (g-i) after 100 cycles, (j-l) after 1000 cycles.

Fig. S18. Elemental energy spectrum of the MnPA electrode scanning area.

Fig. S19. (a-b) SEM image of Fe_2PA_3 electrode piece in the initial state. (c-d) SEM image of the Fe_2PA_3 electrode piece after 100 cycles.

Fig. S20. (a-c) The solubility tests of MnPA-based electrode Before test (soaking in dimethyl carbonate (DMC)). (d-f) The solubility tests of MnPA-based electrode after 200 cycles (soaking in dimethyl carbonate (DMC)).

Fig. S21. (a) CV curves of SnPA anode at different scan rates from 0.1 to 0.4 mV s^{-1}. (b) The linear relationship between log (peak current) and log (scan rate). (c) and the corresponding contribution rate at different scan rates. (d) The contribution of pseudocapacitance to the total current at a scan rate of 0.1 mV s^{-1}.

Fig. S22. (a) CV curves of Fe_2PA_3 negative electrode at different scan rates of 0.1-0.5 mV s^{-1}. (b) The linear relationship between log (peak current) and log (scan rate). (c) and the corresponding contribution rates of pseudocapacitance and diffusion at different scan rates. (d) The contribution of pseudocapacitance to the total current at a sweep speed of 0.1 mV s^{-1}.

Fig. S23. MnPA shows the contribution of pseudocapacitance to the total current at different sweep speeds.

Fig. S24. (a) EIS of SnPA electrodes at different temperatures. (b) Plots of $\ln(T/R_{ct})$ and $1000/T$ for SnPA electrode.

Fig. S25. (a) EIS of Fe_2PA_3 electrode at different temperatures, (b) $\ln(T/R_{ct})$ and $1000/T$ diagrams.

Fig. S26. (a) GITT curves of the SnPA anode during discharge and charging. (b) Lithium-ion diffusion coefficients calculated during the corresponding discharge and charging processes.

Fig. S27. GITT curves of Fe_2PA_3 electrode during discharge and charge and lithium-ion diffusion coefficients calculated during discharge and charge.

Fig. S28. Differential capacitance curves of (a) MnPA//LFP, (b) SnPA//LFP, and (c) $Fe2PA_3$//LFP full batteries at different rates.

Table S1. XPS elemental analysis values of MnPA, SnPA, Fe_2PA_3.

Table S2. ICP elemental analysis data for MnPA, SnPA, Fe_2PA_3.

Table S3. Summarizations of XPS peaks for MnPA, SnPA, and Fe_2PA_3.

Table S4. Mn^{2+}, Fe^{3+}, Sn^{2+} ionic radius.

Table S5. R_b and R_{ct} of Li//SnPA battery at different cycles.

Table S6. Analysis of elemental content in the scanned area.

Table S7. Selected coordination compounds and carboxyl-based-MOFs used directly as anode materials for LIBs.

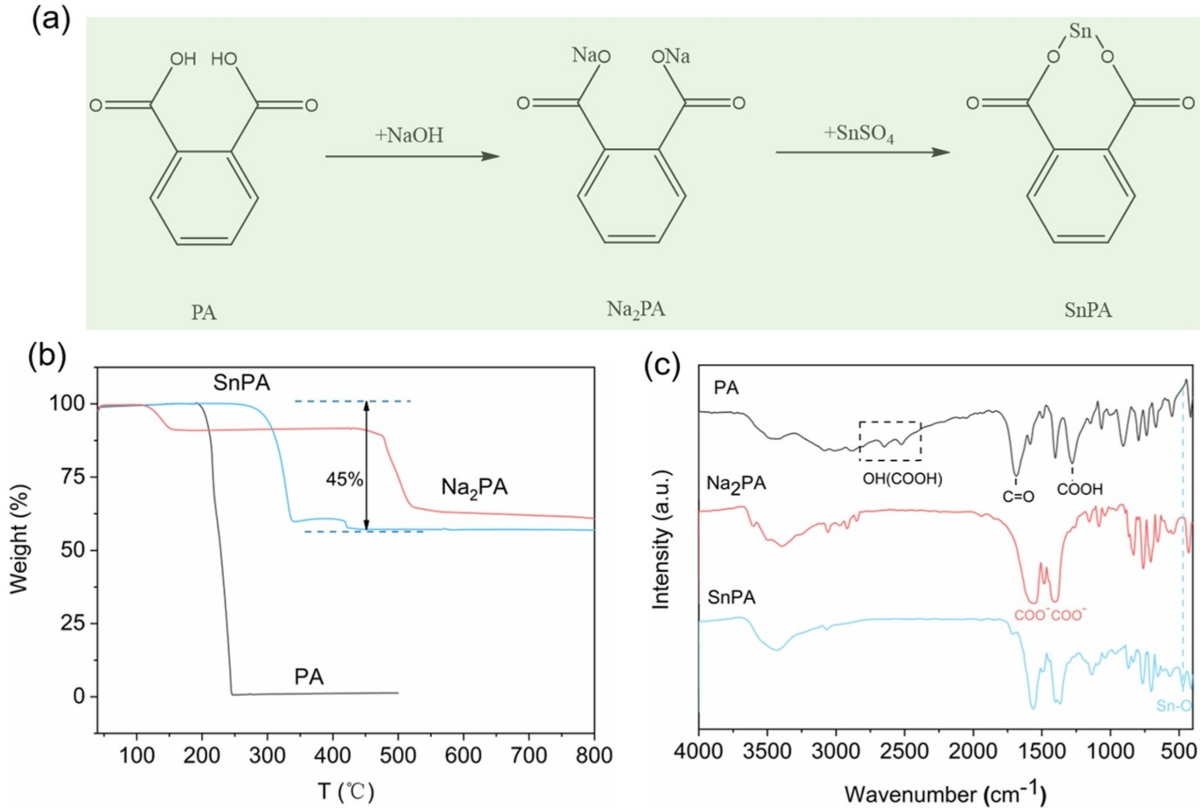

Figure S1. (a) Synthesis path diagram of SnPA. (b) Air atmosphere TGA curves of PA, Na_2PA and SnPA. (c) FT-IR spectra of PA, Na_2PA and SnPA.

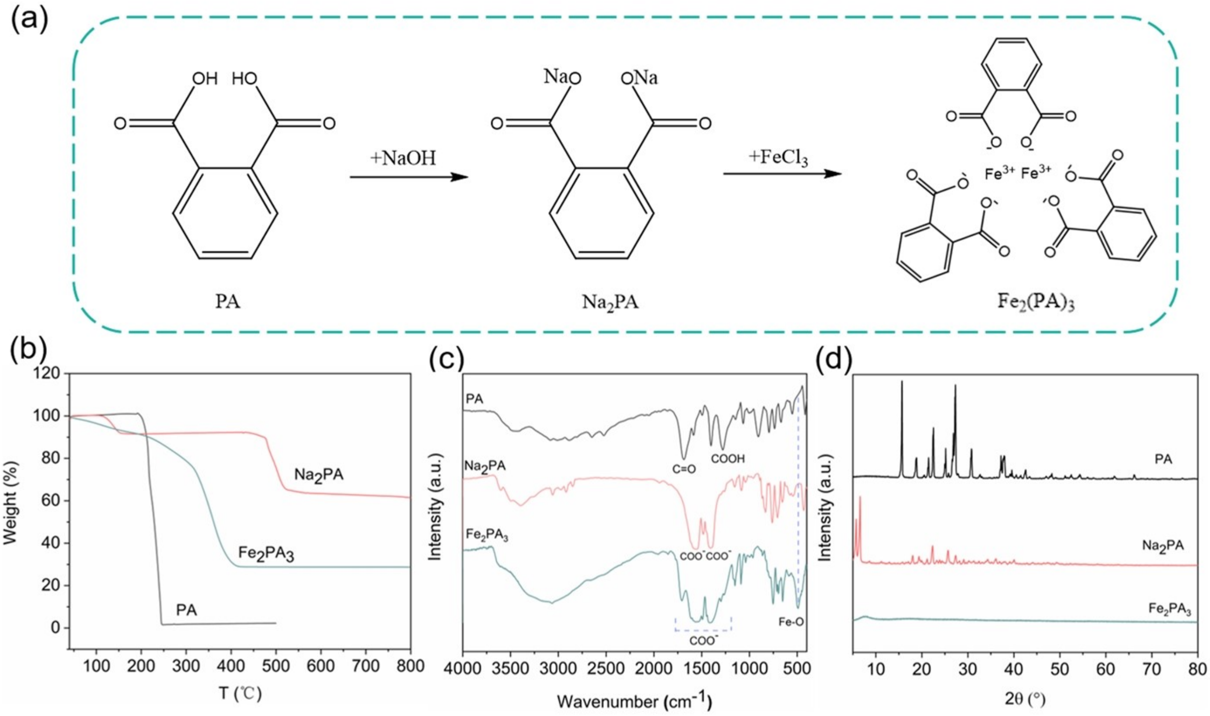

Figure S2. (a) Synthesis pathway diagram of Fe_2PA_3. (b) TGA profile, (c) FT-IR spectra, and (d) XRD pattern of materials along the synthesis pathway.

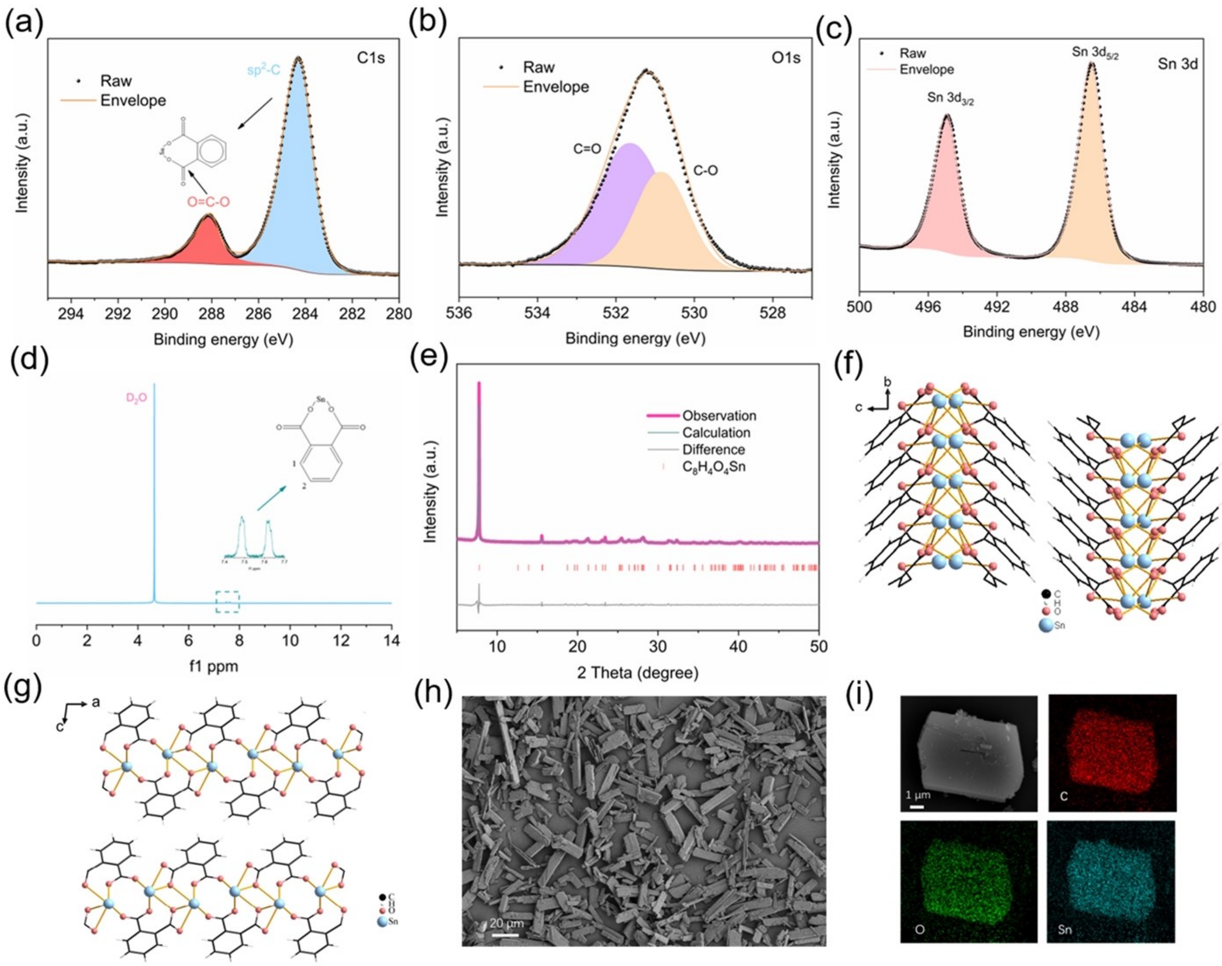

Figure S3. XPS spectra of (a) C 1s, (b) O 1s, and (c) Sn 3d of SnPA. (d) ^{1}H-NMR spectra of SnPA. (e) XRD patterns of SnPA and Rietveld refined XRD patterns. (f) View of SnPA crystal structure as observed from the a-axis. (g) View of SnPA crystal structure as observed from the b-axis. (h) SEM image of SnPA, (i) corresponding EDS.

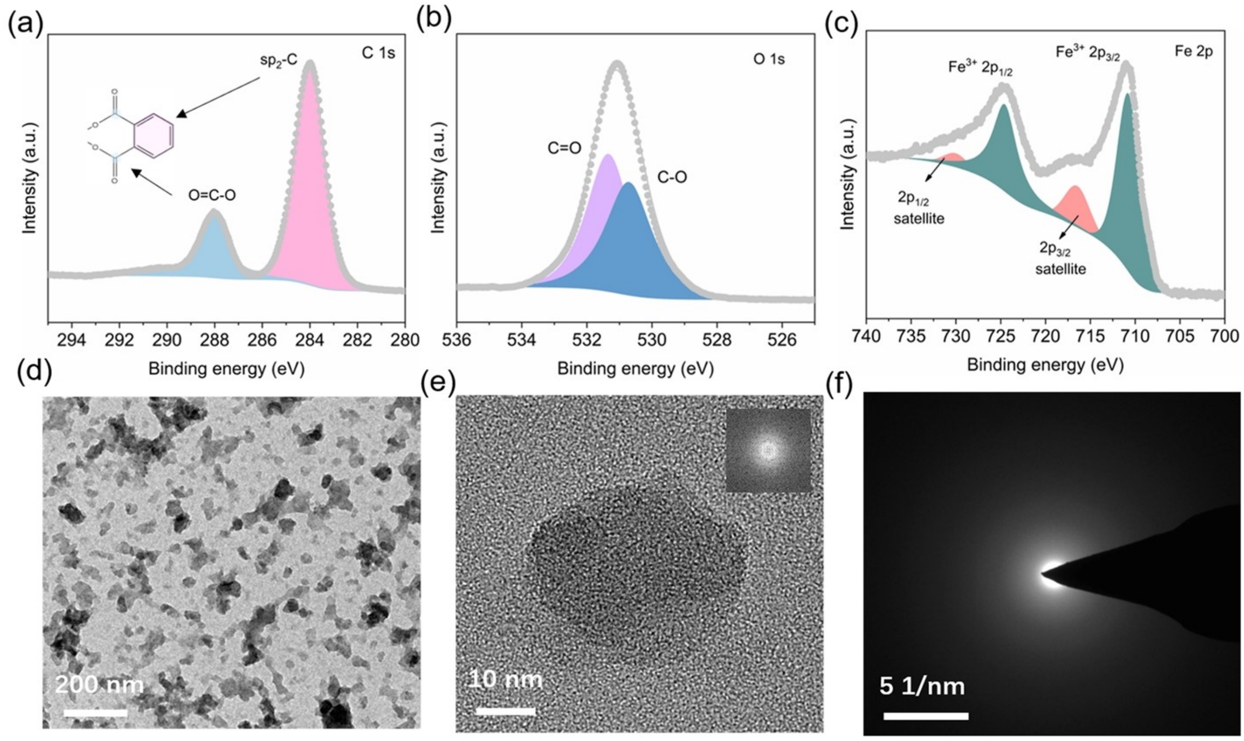

Figure S4. XPS spectra of (a)C 1s, (b) O 1s, (c) Fe 2p of Fe_2PA_3. (d) Morphology of Fe_2PA_3 under TEM. (e) High-resolution HRTEM image of Fe_2PA_3. (f) SAED image of Fe_2PA_3.

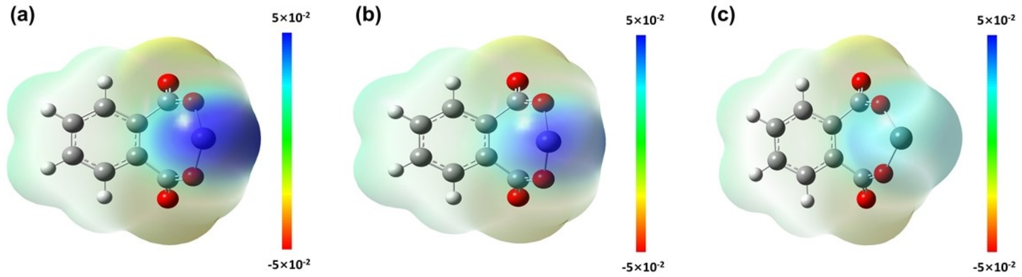

Figure S5. Molecular electrostatic potential (MESP) plots for (a) MnPA and (b) Fe_2PA_3 and (c) SnPA (atoms in light gray, white, red, dark blue, blue, green represent C, H, O, Mn, Fe, Sn respectively).

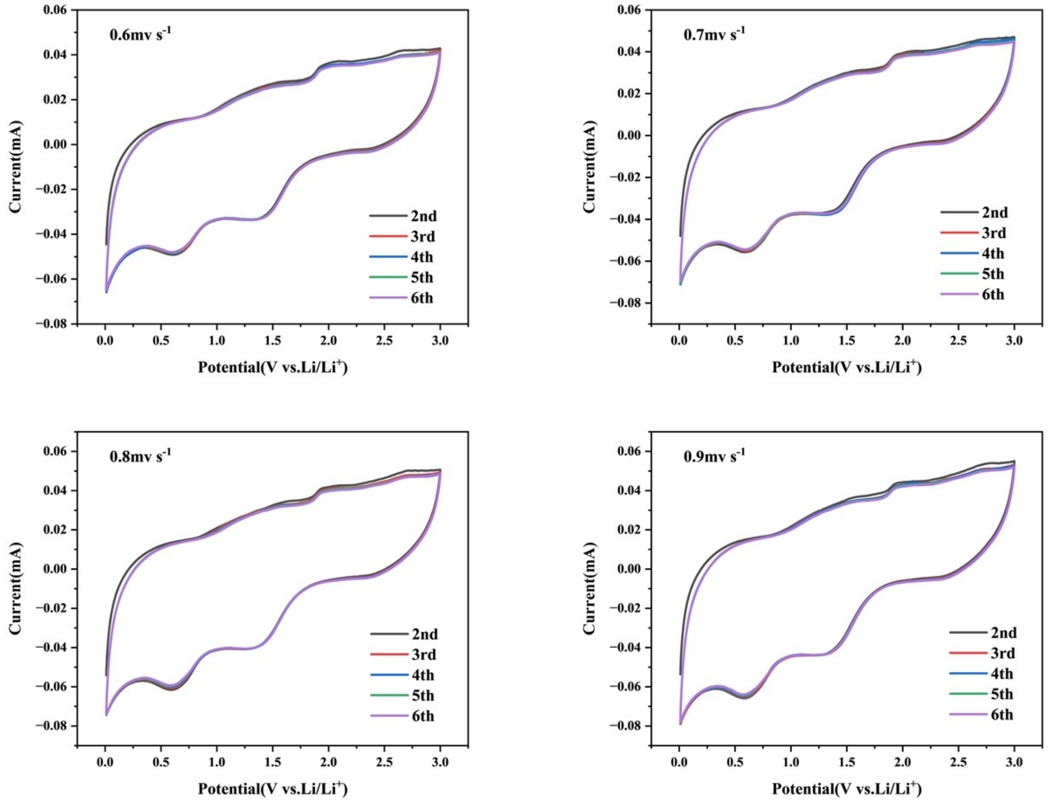

Figure S6. CV curves of the MnPA-based electrodes (scan rates of 0.6, 0.7, 0.8, 0.9 mV s^{-1}, respectively).

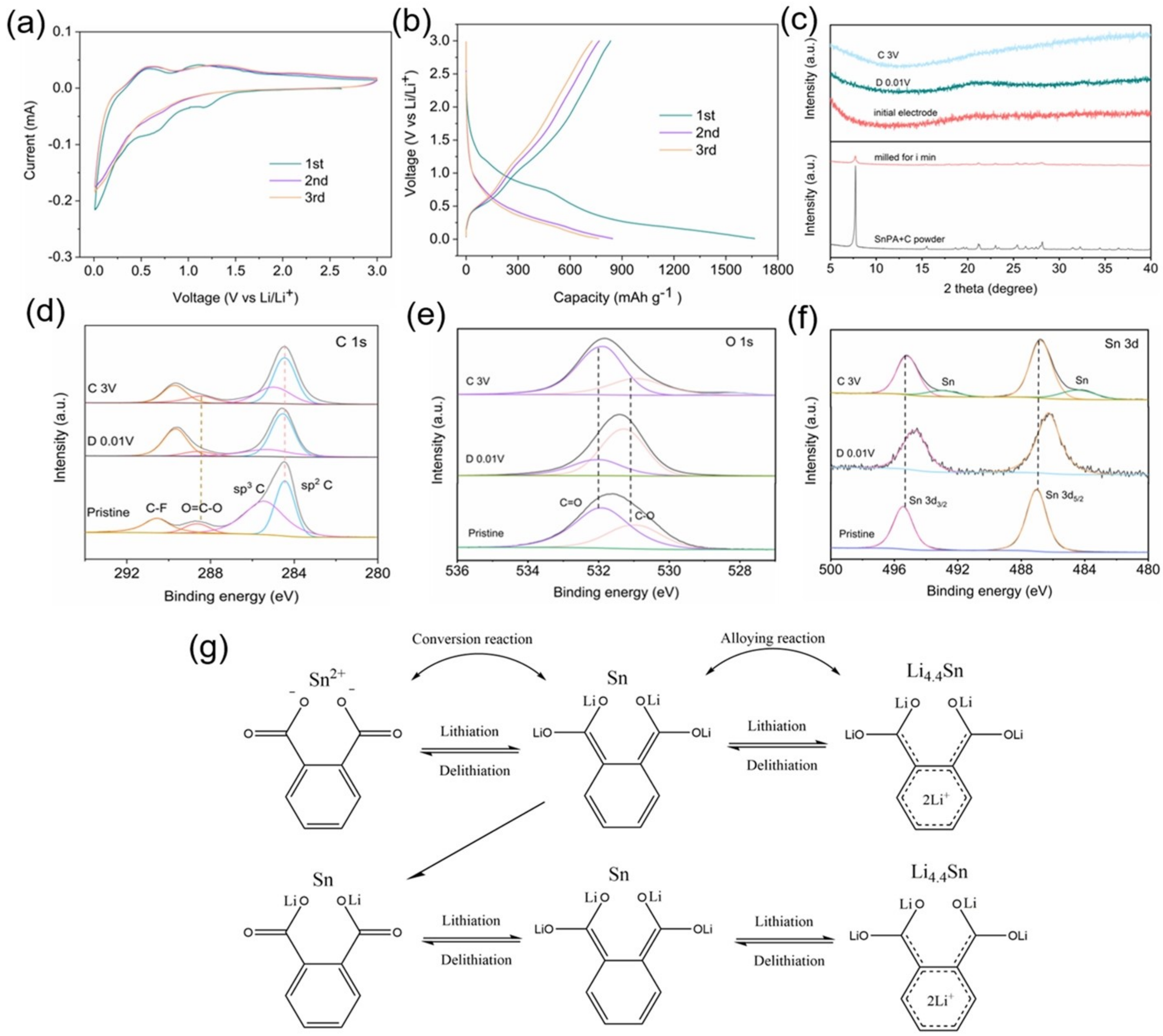

Figure S7. (a) CV curves of the first three turns of the SnPA electrode (scan rate 0.1 mV s^{-1}). (b) GCD curves of the SnPA electrode at 100 mA g^{-1} for the first three cycles. (c) XRD patterns of SnPA mixed with carbon material (bottom half) and ex-situ XRD test of SnPA electrode (top half). (d) C 1s, (e)O 1s, and (f) Sn 3d spectra of Ex-situ XPS. (g) Lithium storage mechanism of SnPA in lithium-ion batteries.

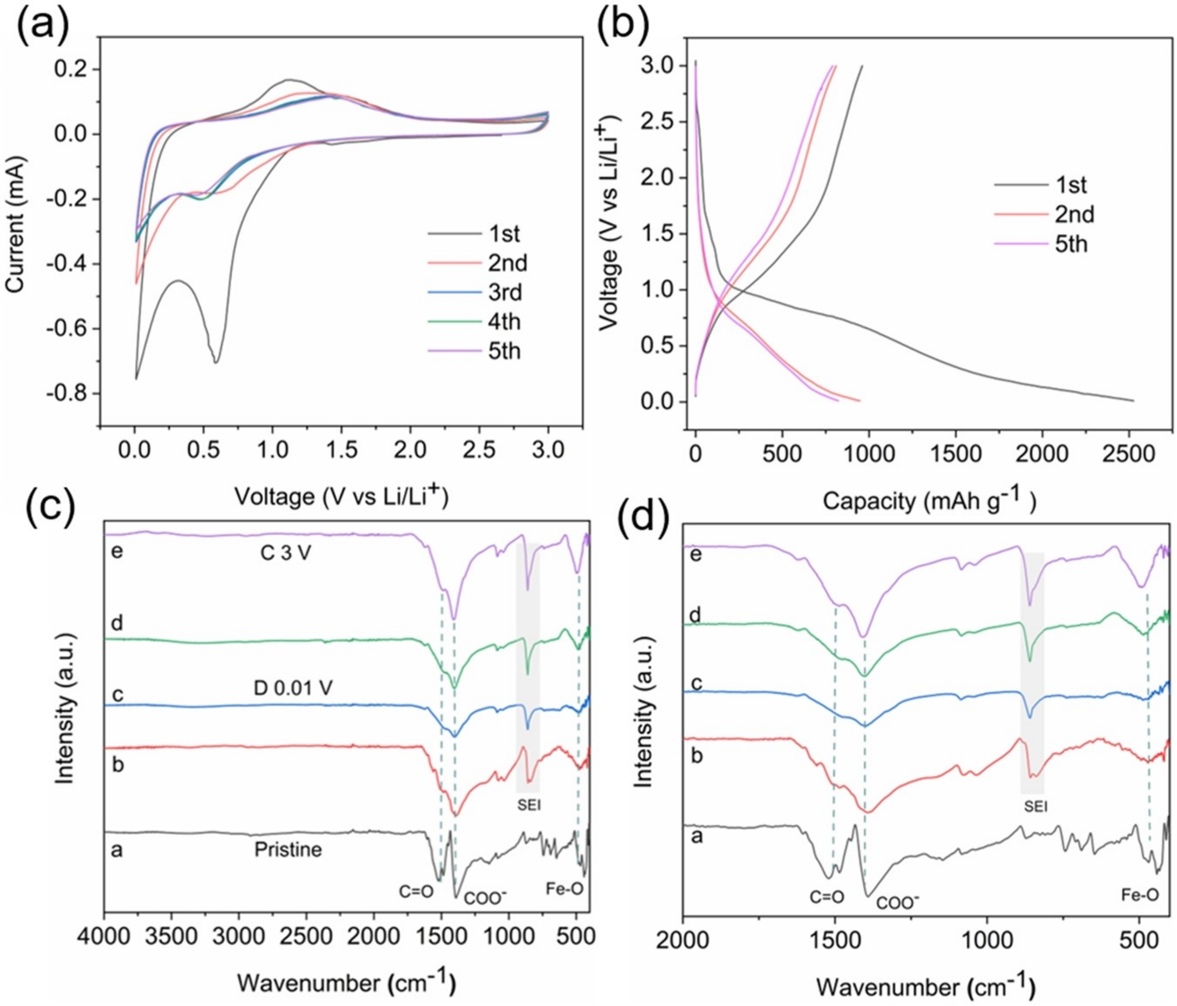

Figure S8. (a) The first three turns of the Fe_2PA_3-based electrode were CV curves (scan rate 0.1 mV s^{-1}). (b) The GCD curves of Fe_2PA_3 electrode at 100 mA g^{-1} for the first five cycles. (c) Ex-situ FT-IR spectra of Fe_2PA_3 electrodes, (d) Enlarged view of ex-situ FT-IR spectra.

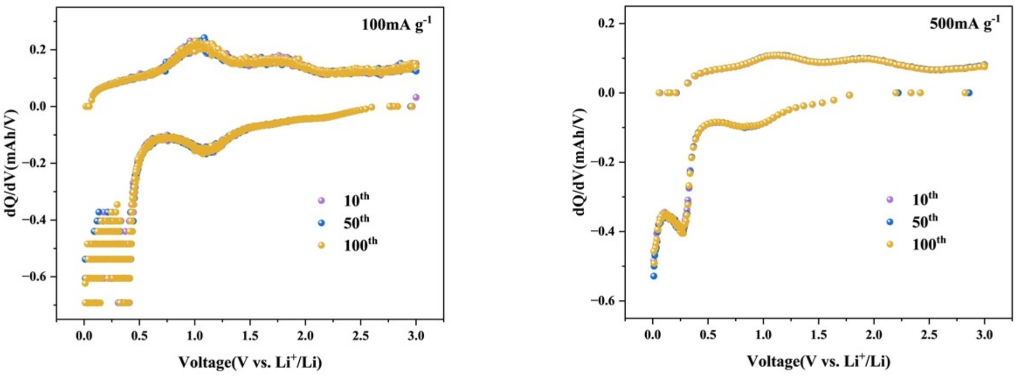

Figure S9. dQ/dV curves of Li//MnPA battery at different current densities.

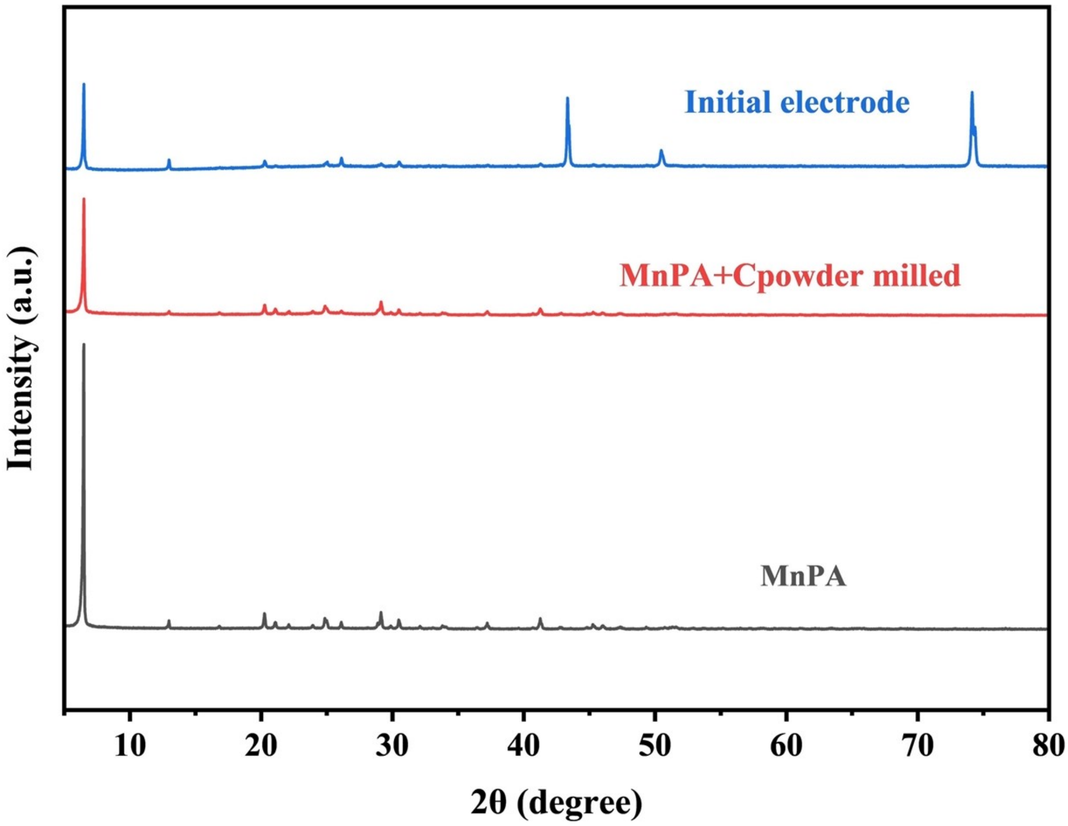

Figure S10. XRD patterns of MnPA, MnPA mixed with carbon material, MnPA initial electrode.

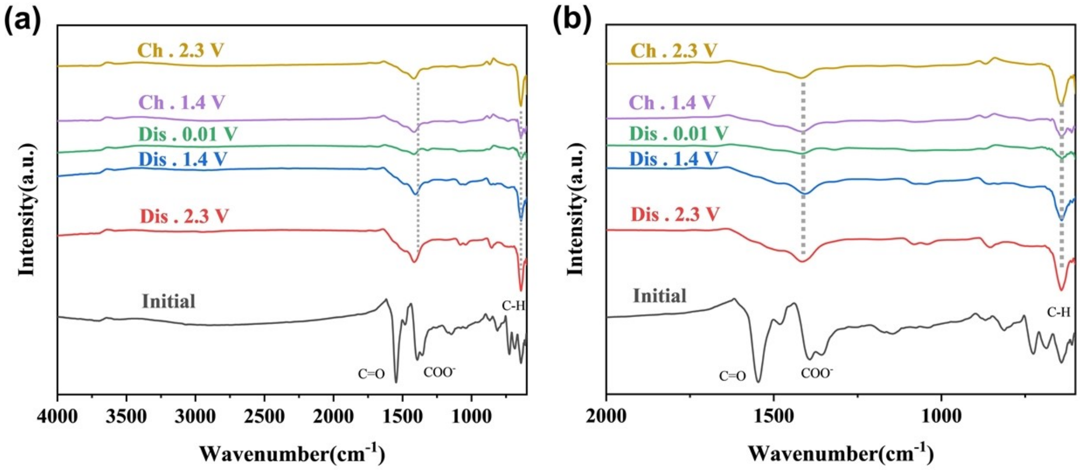

Figure S11. (a) Ex-situ FT-IR spectra of MnPA electrodes, (b) Enlarged view of ex-situ FT-IR spectra.

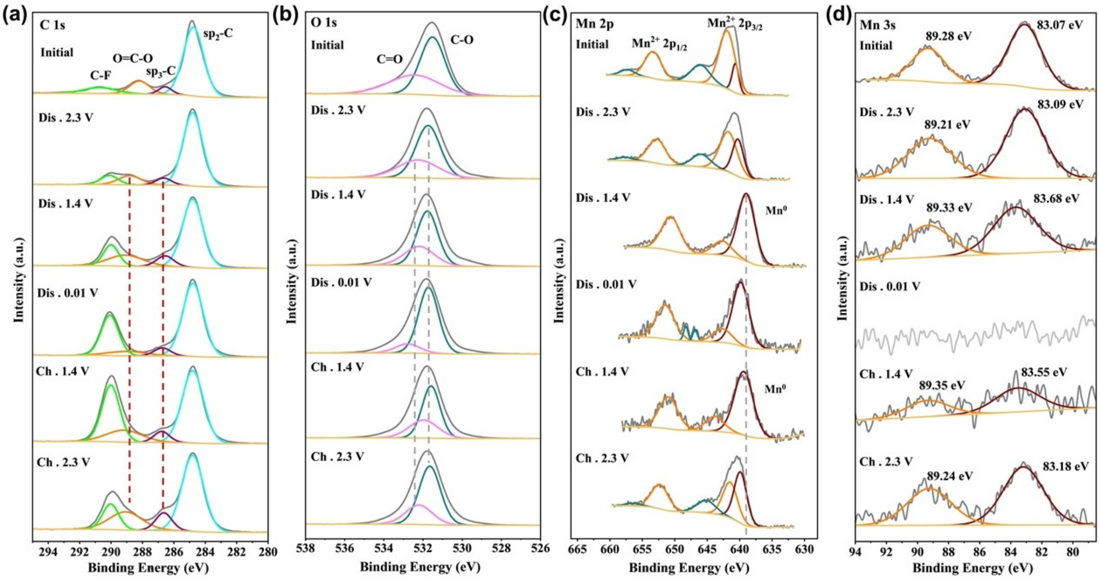

Figure S12. Ex-situ XPS of (a) C 1s, (b) O 1s, (c) Mn 2p, and (d) Mn 3s of MnPA electrodes.

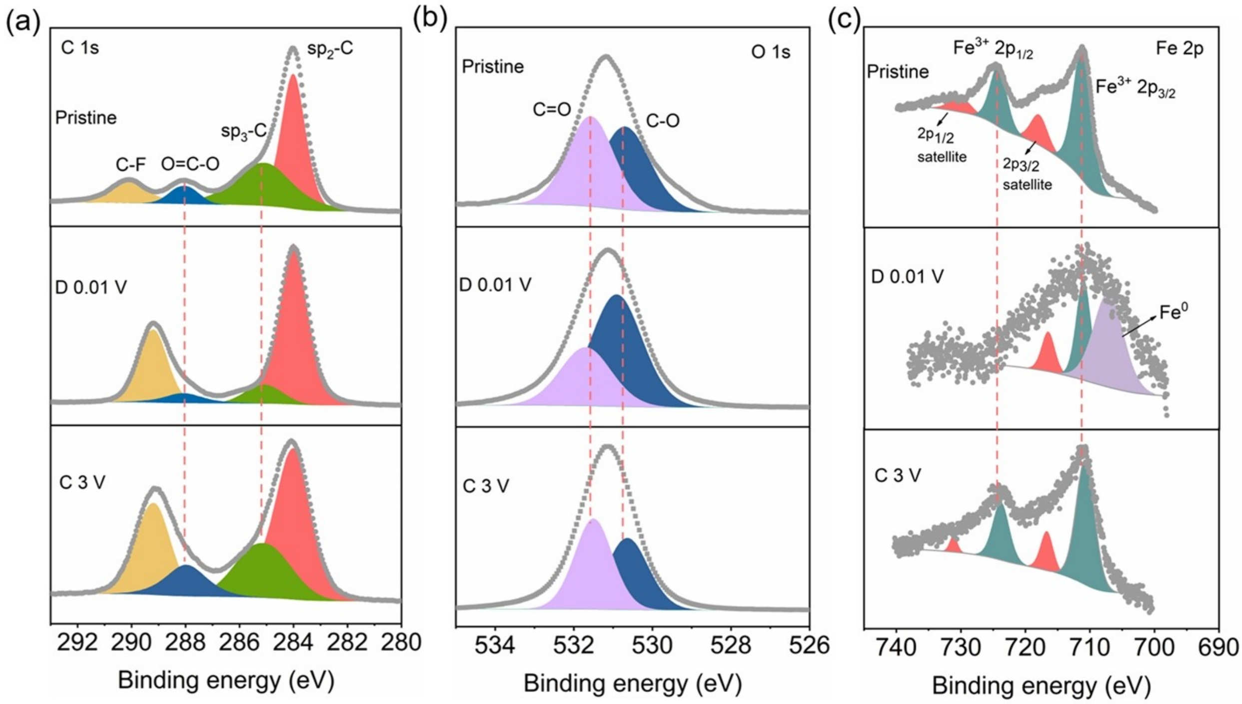

Figure S13. Ex-situ XPS of (a) C 1s, (b) O 1s, and (c) Fe 2p of Fe_2PA_3.

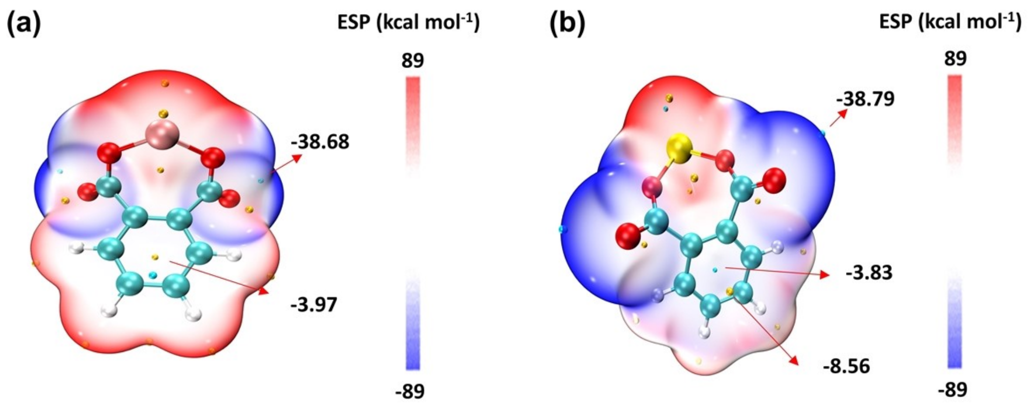

Figure S14. Molecular electrostatic potential (MESP) plots for (a) Fe_2PA_3 and (b) SnPA (atoms in light blue, gray, red, brown, yellow represent C, H, O, Fe, Sn, respectively).

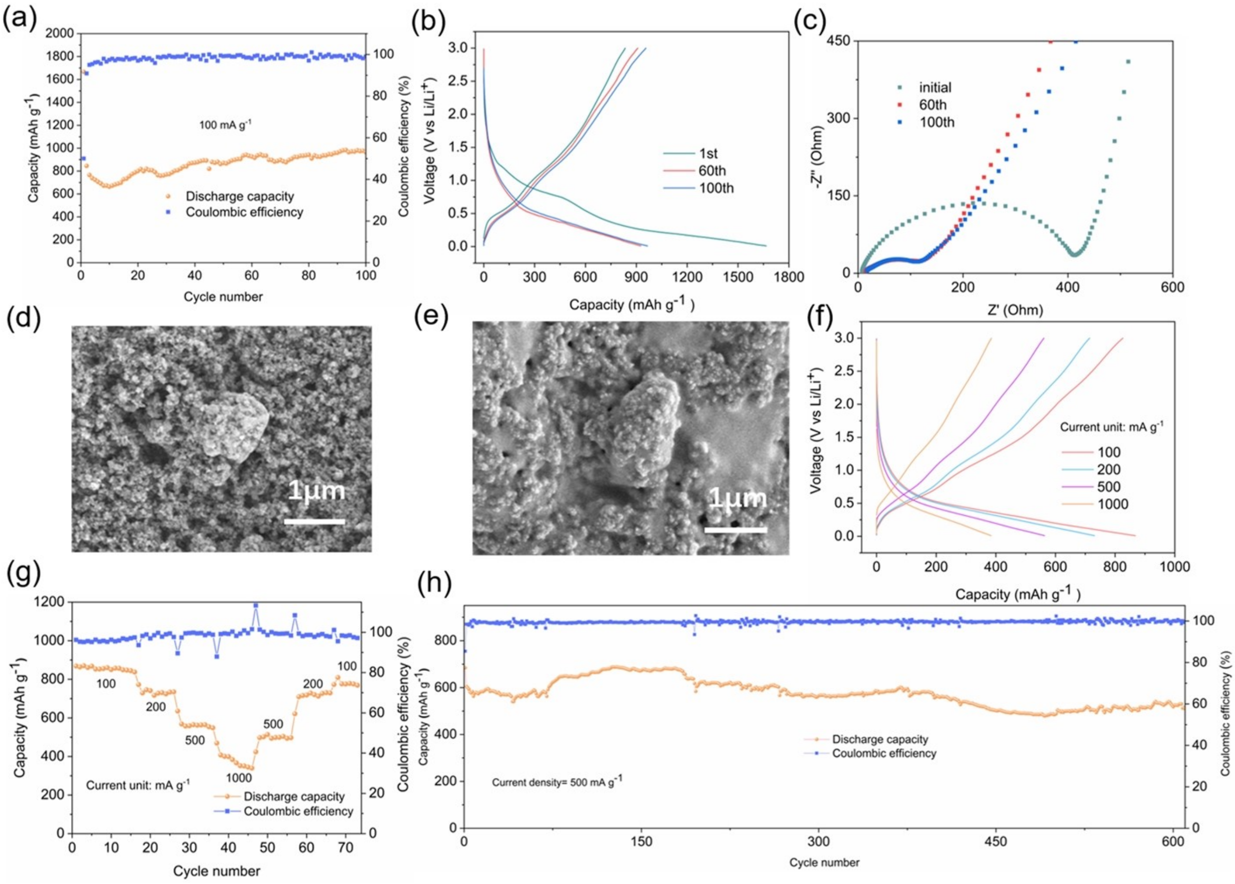

Figure S15. (a-b) Long-cycle performance and GCD curves of the SnPA anode at 100 mA g^{-1}. (c) EIS of SnPA electrode at different cycle number. (d) SEM image of the SnPA-based electrode in the initial state. (e) SEM image of the SnPA-based electrode after 100 cycles. (f) Rate charge-discharge curves. (g) Rate performance of SnPA. (h) Long-cycle performance of the SnPA anode at 500 mA g^{-1}.

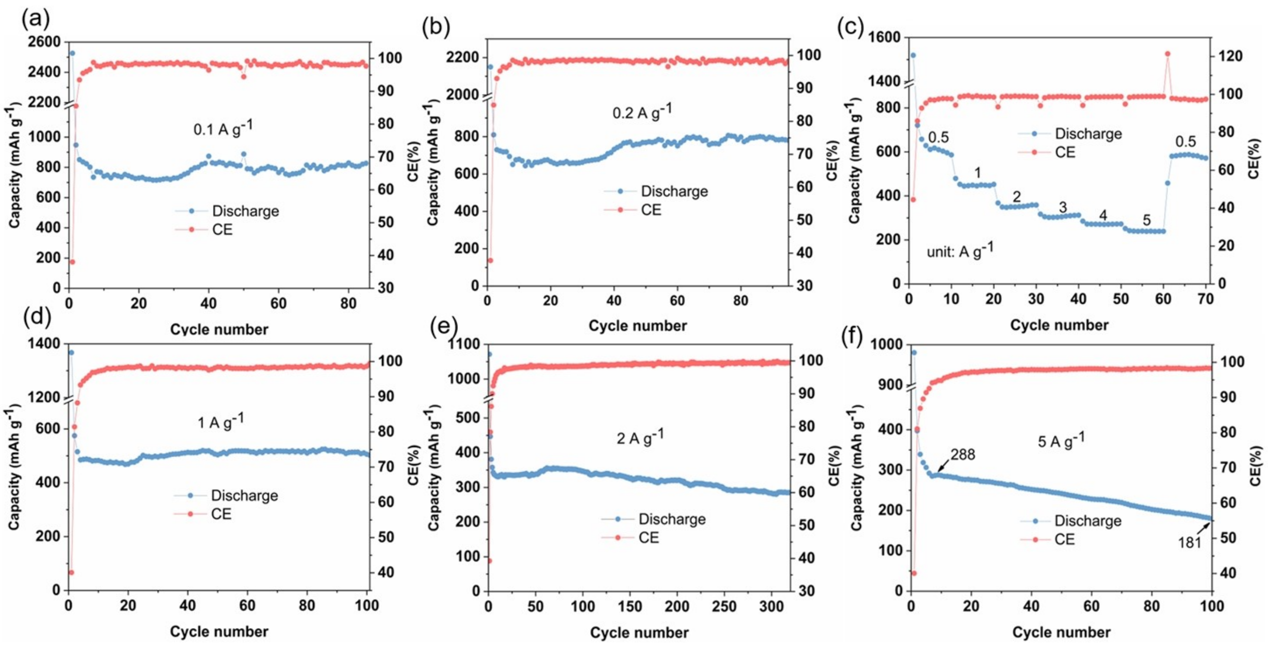

Figure S16. Long-cycle performance of Fe_2PA_3 electrode (a) at 0.1 A g^{-1}. (b) Long-cycle performance at 0.2 A g^{-1}. (c) Rate performance. (d) Long-cycle performance at 1 A g^{-1}. (e) Long-cycle performance at 2 A g^{-1}. (f) Long cycles at 5 A g^{-1}.

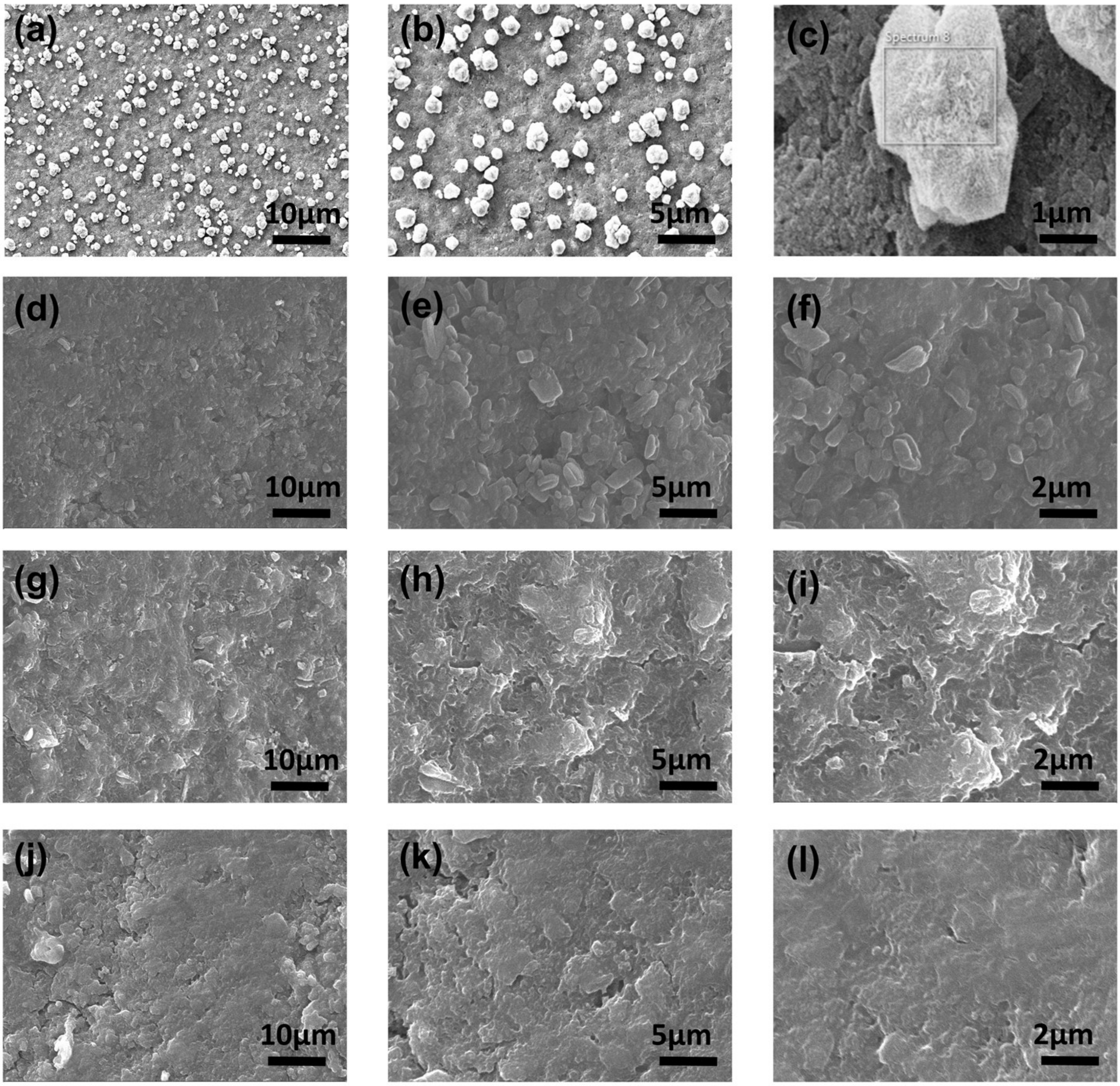

Figure S17. SEM images of MnPA electrode (a-c) before test, (d-f) after 15 cycles, (g-i) after 100 cycles, (j-l) after 1000 cycles.

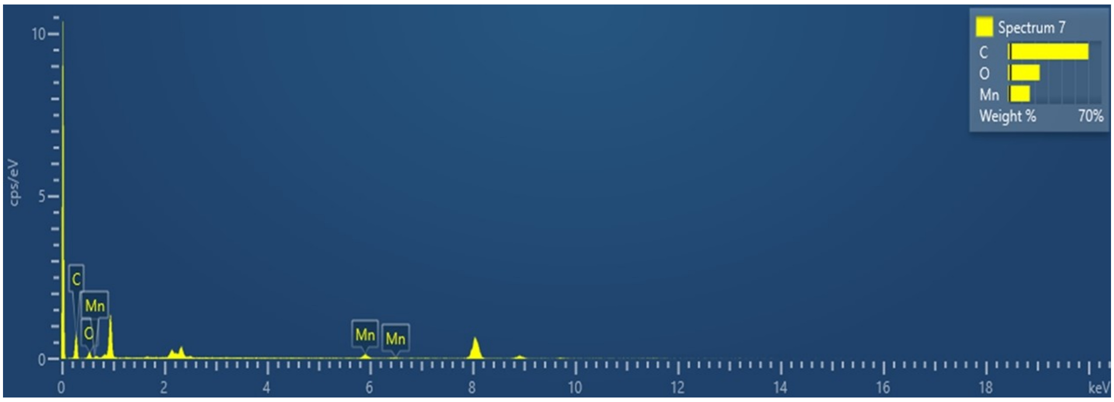

Figure S18. Elemental energy spectrum of the MnPA electrode scanning area.

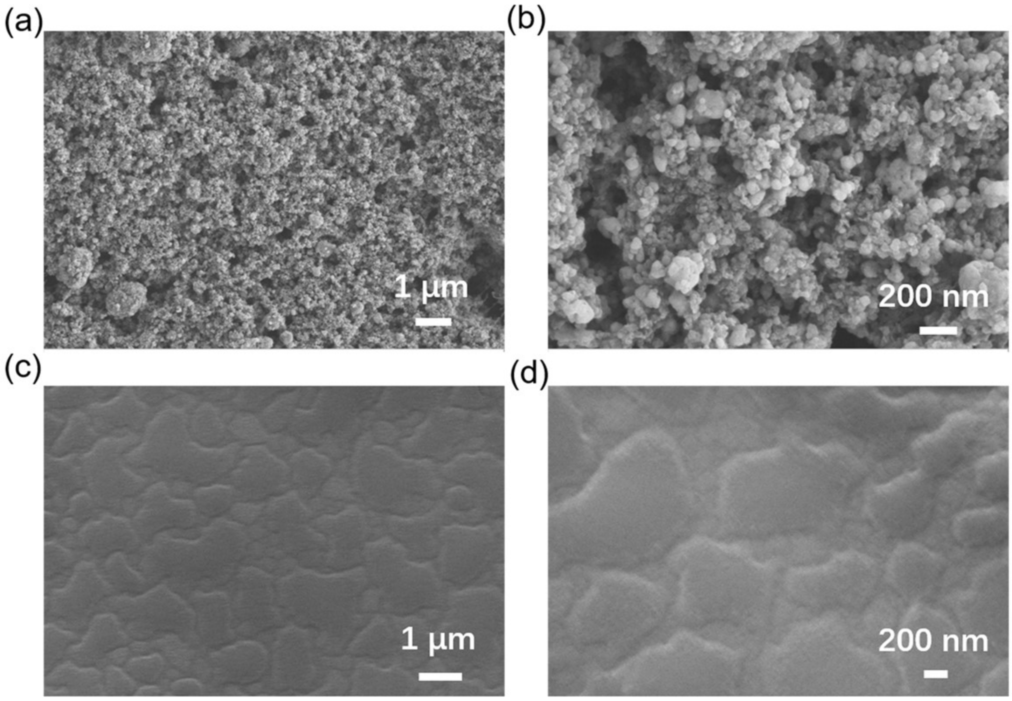

Figure S19. (a-b) SEM image of Fe_2PA_3 electrode piece in the initial state. (c-d) SEM image of the Fe_2PA_3 electrode piece after 100 cycles.

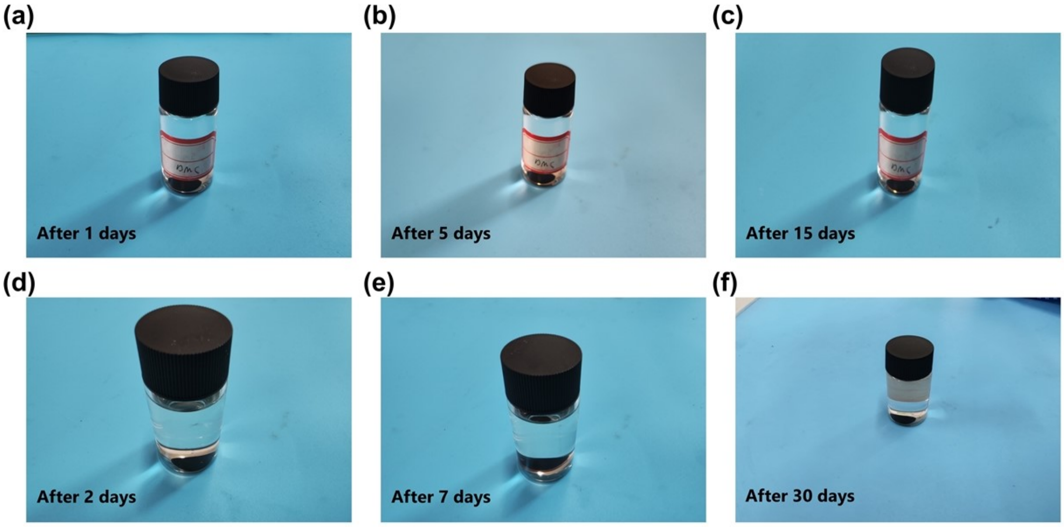

Figure S20. (a-c) The solubility tests of MnPA-based electrode Before test (soaking in dimethyl carbonate (DMC)).

(d-f) The solubility tests of MnPA-based electrode after 200 cycles (soaking in dimethyl carbonate (DMC)).

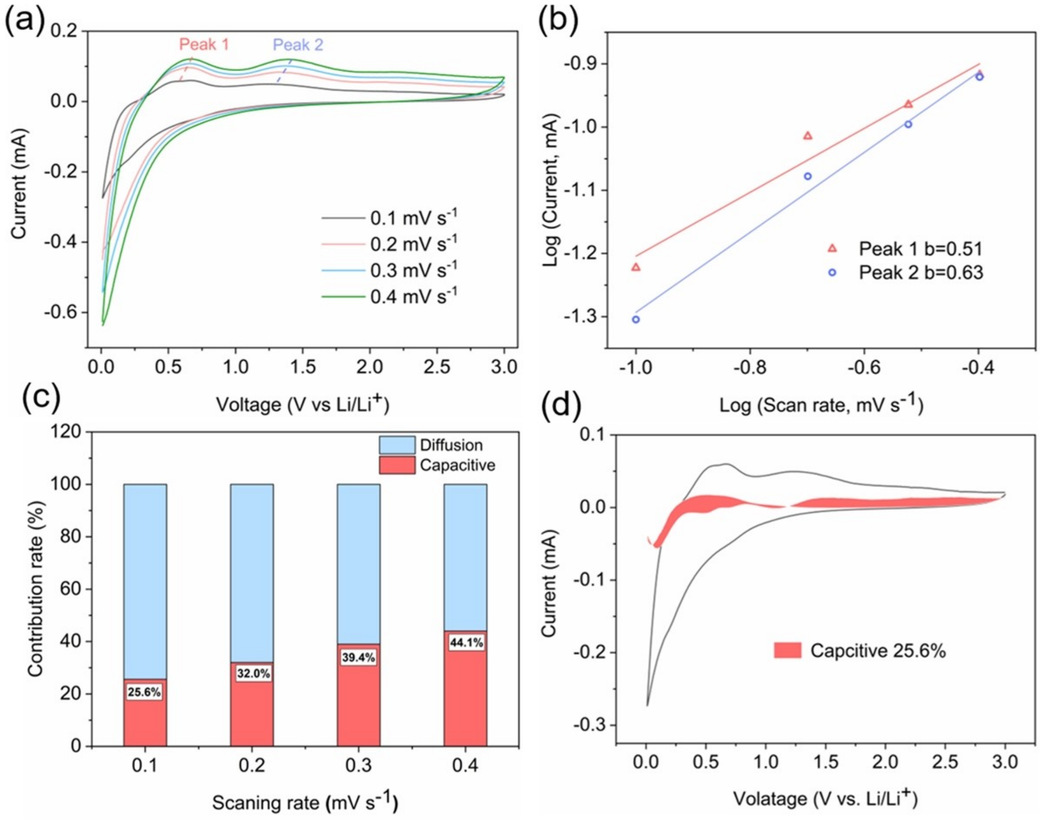

Figure S21. (a) CV curves of SnPA anode at different scan rates from 0.1 to 0.4 mV s^{-1}. (b) The linear relationship between log (peak current) and log (scan rate). (c) and the corresponding contribution rate at different scan rates. (d) The contribution of pseudocapacitance to the total current at a scan rate of 0.1 mV s^{-1}.

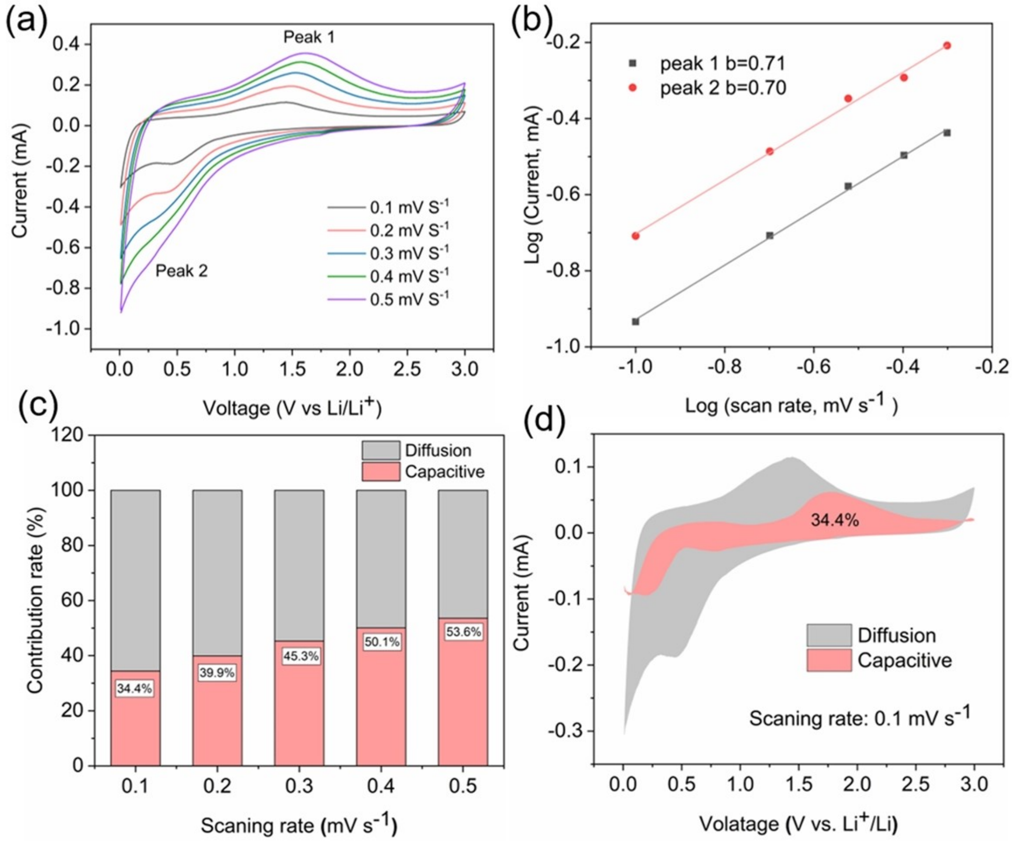

Figure S22. (a) CV curves of Fe_2PA_3 negative electrode at different scan rates of 0.1-0.5 mV s^{-1}. (b) The linear relationship between log (peak current) and log (scan rate). (c) and the corresponding contribution rates of pseudocapacitance and diffusion at different scan rates. (d) The contribution of pseudocapacitance to the total current at a sweep speed of 0.1 mV s^{-1}.

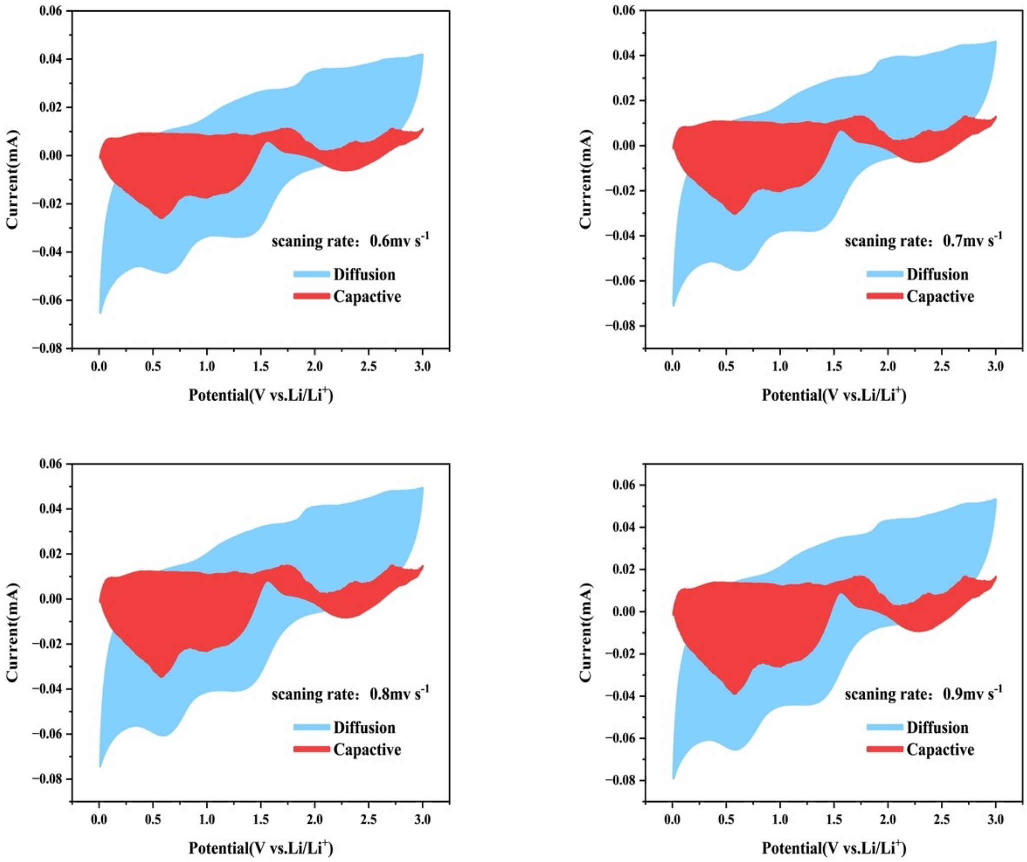

Figure S223. MnPA shows the contribution of pseudocapacitance to the total current at different sweep speeds.

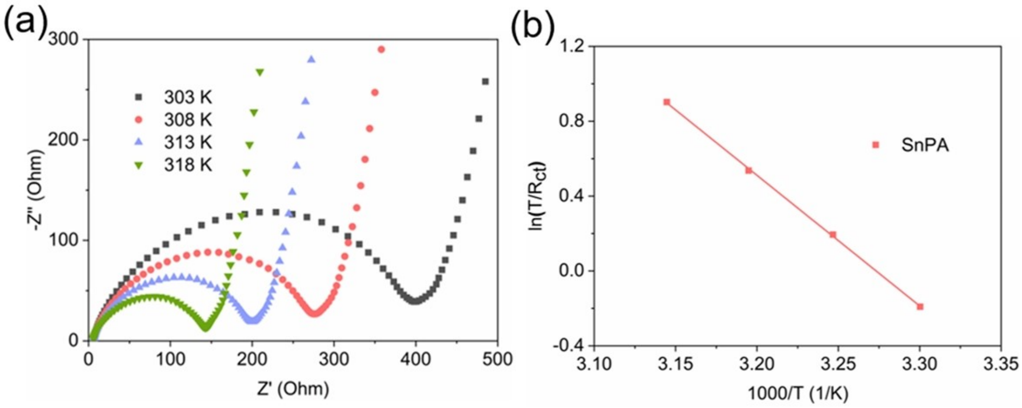

Figure S24. (a) EIS of SnPA electrodes at different temperatures. (b) Plots of ln(T/R_{ct}) and 1000/T for SnPA electrode.

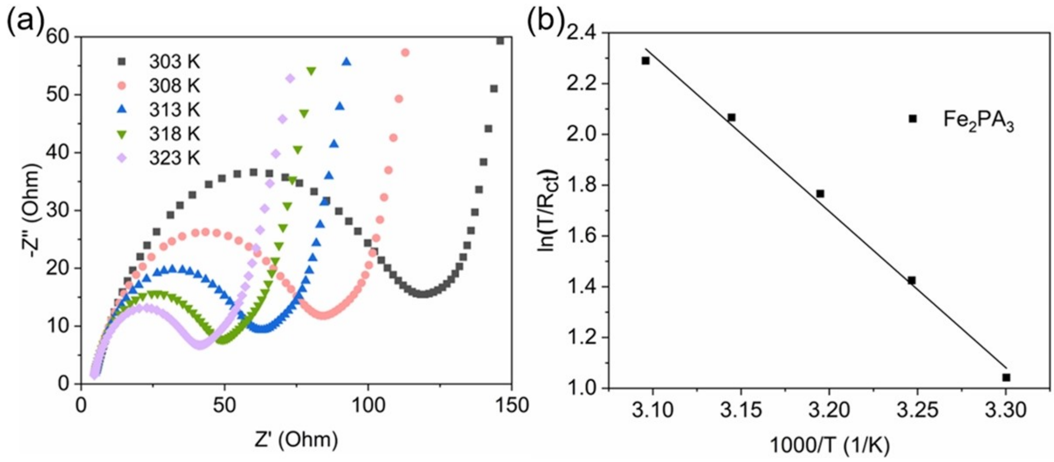

Figure S25. (a) EIS of Fe_2PA_3 electrode at different temperatures, (b) ln(*T/Rct*) and 1000/*T* diagrams.

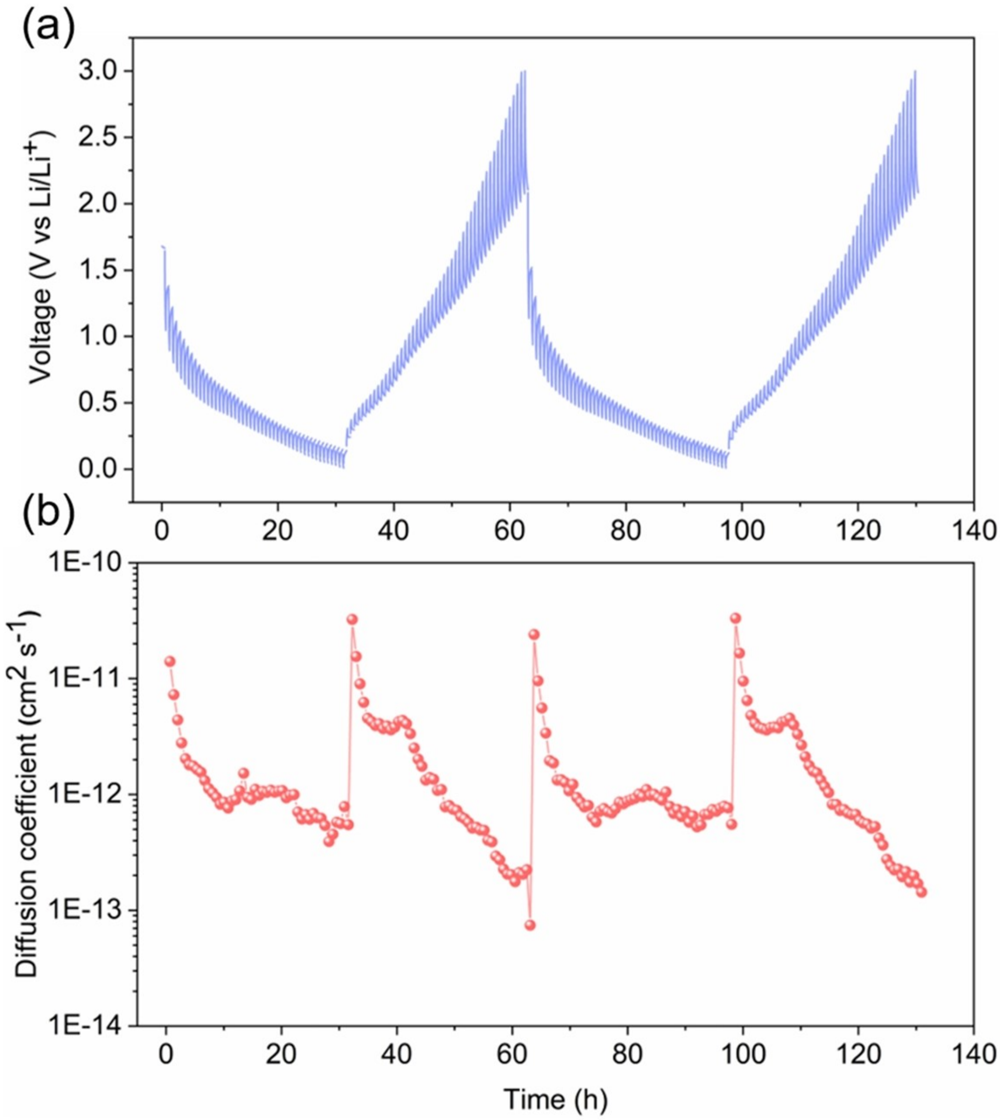

Figure S26. (a) GITT curves of the SnPA anode during discharge and charging. (b) Lithium-ion diffusion coefficients calculated during the corresponding discharge and charging processes.

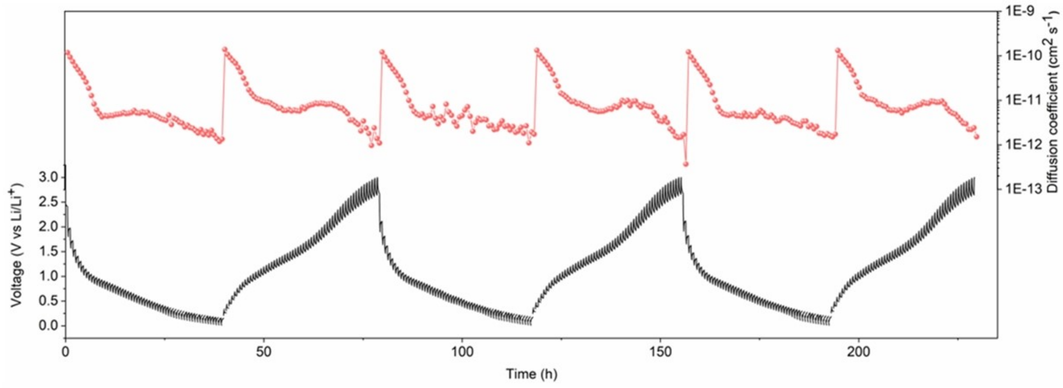

Figure S27. GITT curves of Fe_2PA_3 electrode during discharge and charge and lithium-ion diffusion coefficients calculated during discharge and charge.

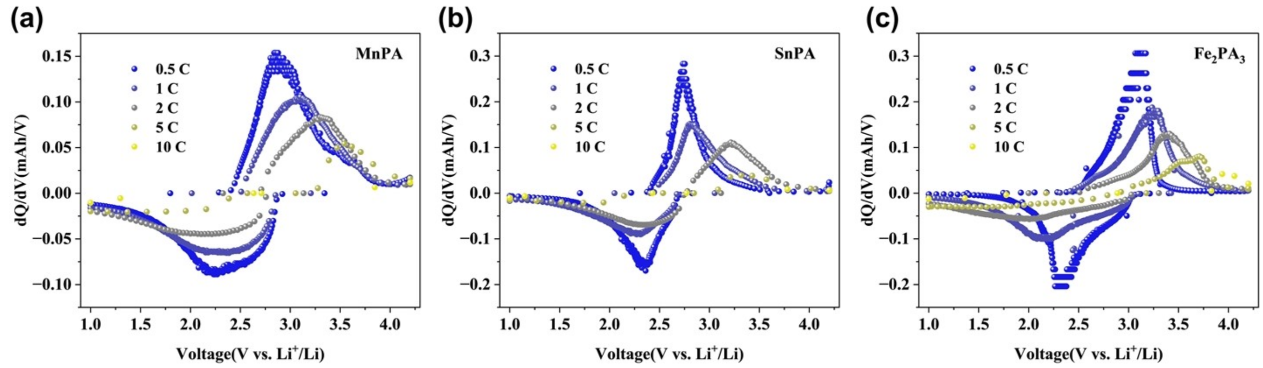

Figure S28. Differential capacitance curves of (a) MnPA//LFP, (b) SnPA//LFP, and (c) Fe_2PA_3//LFP full batteries at different rates.

Table S1. XPS elemental analysis values of MnPA, SnPA, Fe_2PA_3.

element	MnPA	SnPA	Fe_2PA_3
C	62.43%	34.87%	48.80%
O	22.37%	23.23%	32.68 %
Mn	15.20%		
Sn		41.90%	
Fe			18.52%

Table S2. ICP elemental analysis data for MnPA, SnPA, Fe_2PA_3.

Material	M_0 (g)	V_0(mL)	Test element	C_0 (mg/L)	LOD (mg/L)	f	C_1 (mg/L)	C_x (mg/kg)	AVG (mg/kg)	W(%)
MnPA	0.02464	50	Na	1.0151	<0.01	1	1.01510	2059.86	2.04E+03	0.204%
	0.02509	50		1.0140		1	1.01400	2020.73		
SnPA	0.02646	50	Na	5.9951	<0.01	1	5.99510	11328.61	1.13E+04	1.13%
	0.02951	50		6.6132		1	6.61320	11205.02		
Fe_2PA_3	0.02475	50	Na	2.2394	<0.01	5	11.19700	22620.20	2.27E+04	2.27%
	0.02436	50		2.2183		5	11.09150	22765.80		

$$C_x(mg/kg) = \frac{C_0(mg/L) * f * V_0(mL) * 10^{-2}}{m(g) * 10^{-2}} = \frac{C_1(mg/L) * V_0(mL) * 10^{-2}}{m(g) * 10^{-2}} \tag{1}$$

$$W(\%) = \frac{C_x(mg/kg)}{10^6} * 100\% \tag{2}$$

Where M_0 is the mass of the sample taken when analyzing the sample (g); V_0 is the constant volume of the sample after digestion (mL); f is the dilution; C_0 is the concentration of the element in the test solution (mg/L); C_1 is the element concentration of the sample digestion solution (mg/L, C1(mg/L)=CO(mg/L)*f)； C_x is the final test result of the element under test (mg/kg); W(%) is the final test result of the tested element, expressed as a percentage.

Table S3. Summarizations of XPS peaks for MnPA, SnPA, and Fe_2PA_3.

Name		MnPA	SnPA	Fe_2PA_3
			Peak(eV)	
C 1s	sp^2 C	284.80	284.40	284.00
	O=C-O	288.54	288.50	288.00
O 1s	C-O	531.50	530.60	530.44
	C=O	532.00	531.70	531.30

Table S4. Mn^{2+}, Fe^{3+}, Sn^{2+} ionic radius.[1]

Name	**Mn^{2+}**	**Fe^{3+}**	**Sn^{2+}**
ionic radius(pm)	84	64	93

Table S5. R_b and R_{ct} of Li//SnPA battery at different cycles.

Cycle number	$R_b(\Omega)$	$R_{ct}(\Omega)$
initial	5.67	385.5
60	10.33	92.5
100	12.8	88.2

Table S6. Analysis of elemental content in the scanned area.

Element	Wt%	Atomic %
C	60.16	73.88
O	23.60	21.76
Mn	16.24	4.36

Table S7. Selected coordination compounds and carboxyl-based-MOFs used directly as anode materials for LIBs.

Material	Capacity (mAh g^{-1})/Current density(A g^{-1}) /Cycle number	Voltage (V)	Ref.
Mn-LCP	390/0.05/50	0.01−3.0	2
FOR_2	406/0.1/70	0.01−3.0	3
$Zn_3(HCOO)_6$	560/0/06/60	0.005−3.0	3
$Co_2(OH)_2BDC$	540/0.1/50	0.01−2.5	4
Co-PTA	645/0.095/80	0.01−3.0	5
MnBTC	694/0.103/100, 250/2.06/100	0.01−3.0	6
Fe/Zn-BTC	675/0.1/80	0.01−3.0	6
MnCo-T	697/0.2/150	0.01−2.6	7
Li_2PA	610/0.06/130，260/1/500	0.01−3.0	8
Sn2dobdc	1044/0.1/50	0.01−3.0	9
Sn2dobpdc	1099/0.1/45	0.01−3.0	9
$Co_2(DOBDC)$	526.1/0/5/200	0.01−3.0	10
Co(L) MOF/RGO	1185/0.1/50, 639/0.5/120	0.01−3.0	11
r-CoHNta	875/0.5/300	0.01−3.0	12
Mn-LCP	390/0.05/50	0.01−2.5	13
$[Co_3(L_1)(N_3)_4]$	580/0.1/200	0.01−3.0	14
Mn-UMOFNs	1187/0.1/100, 818/1/300	0.01−3.0	15
Ni-UMOFNs	546/0.1/100, 346/1/300	0.01−3.0	15
$AlCl_3$-FumA	170/0.0375/50	0.01−3.0	16
S-Co-MOF	1021/0.1/200, 435/1/1000	0.01−3.0	17
$[Co(C_5O_5)(H_2O)_3]_n$	741/0.1/140, 476/0.5/400	0.01−2.4	18
$[Mn(C_5O_5)(H_2O)_3]_n$	729/0.1/140, 680/0.5/400	0.01−2.4	18
NiFeMn-pma	611/0.1/75	0.01−3.0	19
MnPA	**1100/0.1/90, 300/2/2100**	**0.01−3.0**	**This work**
SnPA	**930/0.1/100, 580/0.5/600**	**0.01−3.0**	**This work**
Fe_2PA_3	**810/0.1/85, 800/0.2/95, 200/5/100**	**0.01−3.0**	**This work**

References

1. D. Ai, R. Zeng and D. Ye, *Science China Chemistry*, 1999, **42**, 337-344.
2. H. W. Song, L. S. Shen, J. Wang and C. X. Wang, *J Mater Chem A*, 2016, **4**, 15411-15419.
3. Kuppan Saravanan, Palani Balaya and Jagadese J. Vittal, *Journal of Materials Chemistry*, 2010, **20**, 8329-8335.
4. L. Gou, L. M. Hao, Y. X. Shi, S. L. Ma, X. Y. Fan, L. Xu, D. L. Li and K. Wang, *Journal of Solid State Chemistry*, 2014, **210**, 121-124.
5. J. Wang, W. Liu, G. Luo, Z. J. Li, C. Zhao, H. R. Zhang, M. Z. Zhu, Q. Xu, X. Q. Wang, C. M. Zhao, Y. T. Qu, Z. K. Yang, T. Yao, Y. F. Li, Y. Lin, Y. Wu and Y. D. Li, *Energ Environ Sci*, 2018, **11**, 3375-3379.
6. H. P. Hu, X. B. Lou, C. Li, X. S. Hu, T. Li, Q. Chen, M. Shen and B. W. Hu, *New J Chem*, 2016, **40**, 9746-9752.
7. H. H. Lee, Y. Park, K.-H. Shin, K. T. Lee and S. Y. Hong, *ACS Applied Materials & Interfaces*, 2014, **6**, 19118–19126.
8. C. Li, Y. Huang, J. Liu, J. Chen, X. Li, M. Wang, B. Guo and Y. Lin, *Journal of Power Sources*, 2022, **546**, 231992.
9. J. W. Liu, D. X. Xie, X. F. Xu, L. Z. Jiang, R. Si, W. Shi and P. Cheng, *Nat Commun*, 2021, **12,** 2400.
10. Y. Q. Ning, X. B. Lou, C. Li, X. S. Hu and B. W. Hu, *Chem-Eur J*, 2017, **23**, 15984-15990.
11. C. F. Dong and L. Q. Xu, *Acs Applied Materials & Interfaces*, 2017, **9**, 7160-7168.
12. J. Du, J. Ren, M. Shu, X. Xu, Z. Niu, W. Shi, R. Si and P. Cheng, *Angewandte Chemie-International Edition*, 2021, **60**, 4142-4149.
13. Z. M. Yang, S. P. Zhao, M. H. Zhang, Z. D. Zhang, T. R. Ma, S. Yuan, J. Su, C. H. Li and J. L. Zuo, *Angewandte Chemie*, 2023, **62**, e202304183..
14. T. Gong, X. B. Lou, E. Q. Gao and B. W. Hu, *Acs Applied Materials & Interfaces*, 2017, **9**, 21839-21847.
15. C. Li, X. S. Hu, W. Tong, W. S. Yan, X. B. Lou, M. Shen and B. W. Hu, *Acs Applied Materials & Interfaces*, 2017, **9**, 29829-29838.
16. K. Wang, J. C. Chen, F. X. Hou, H. Wang, Y. H. Zhang, X. B. Zhong, Y. X. Song, Y. A. Zhang, Z. W. Zhang, H. T. Liu, J. F. Liang and H. Wang, *Chemical Engineering Journal*, 2023, **455**, 140561.
17. X. B. Lou, Y. Q. Ning, C. Li, X. S. Hu, M. Shen and B. W. Hu, *Sci China Mater*, 2018, **61**, 1040-1048.
18. S. X. Ma, L. Shen, Q. Liu, W. Y. Shi, C. Zhang, F. Liu, J. A. Baucom, D. Zhang, H. J. Yue, H. B. Wu and Y. F. Lu, *Acs Applied Materials & Interfaces*, 2020, **12**, 43824-43832.
19. A. T. Zhang, Q. Zhang, H. C. Fu, H. W. Zong and H. W. Guo, *Small*, 2023, **19**, 2303911.